Sulfides and hollows formed on Mercury's surface by reactions with reducing S-rich gases

C. J. Renggli[1*], S. Klemme[1], A. Morlok[2], J. Berndt[1], I. Weber[2], H. Hiesinger[2], P. L. King[3]

[1] Institut für Mineralogie, Westfälische Wilhelms-Universität Münster, Münster, 48149, Deutschland

[2] Institut für Planetologie, Westfälische Wilhelms-Universität Münster, Münster, 48149, Deutschland

[3] Research School of Earth Sciences, The Australian National University, Canberra, 2601, Australia

[*]Corresponding author: Christian Renggli (renggli@uni-muenster.de)

ORCID: Renggli 0000-0001-8913-4176

Keywords

Mercury, Sulfur on Mercury, Sulfidation, Gas-Solid Reactions, Mercury Hollows

This preprint is published in Earth and Planetary Science Letters:

https://doi.org/10.1016/j.epsl.2022.117647

Abstract

The surface of Mercury is enriched in sulfur, with up to 4 wt.% detected by the NASA MESSENGER mission, and has been challenging to understand in the context of other terrestrial planets. We posit, that magmatic S was mobilized as a gas phase in volcanic and impact processes near the surface, exposing silicates to a hot S-rich gas at reducing conditions and allowing conditions for rapid gas-solid reactions. Here we present novel experiments on the reaction of Mercury composition glasses with reduced S-rich gas, forming Ca- and Mg-sulfides. The reaction products provide porous and fragile materials that create previously enigmatic hollows on Mercury. Our model predicts that the gas-solid reaction forms Ca-Mg-Fe-Ti-sulfide assemblages with SiO_2 and aluminosilicates, distinct from formation as magmatic minerals. The ESA/JAXA BepiColombo mission to Mercury will allow this hypothesis to be tested.

Introduction

The NASA MESSENGER spacecraft detected a high abundance of sulfur on the surface of Mercury with up to 4 wt.% (McCoy et al., 2018; Namur et al., 2016a; Nittler et al., 2018, 2011; Weider et al., 2015). The S concentration varies between terranes with the highest values inferred for the high-Mg region (HMR, 2.7 wt.%), intermediate abundances in the low-Mg northern volcanic plains (NP, 1.9 wt.%), and lower abundances in pyroclastic deposits northeast of the Rachmaninoff basin (Vander Kaaden et al., 2017). These elemental concentrations, derived from S/Si element ratios, were independently observed by the X-Ray Spectrometer (Nittler et al., 2011) and the Gamma-Ray Spectrometer (Evans et al., 2012; Nittler et al., 2018). The correlation between Mg and S, as well as Ca and S, suggests the presence of the minerals niningerite (MgS) and oldhamite (CaS) on the planets surface (Cartier and Wood, 2019; Evans et al., 2012).

Constraining the origin of the exceptionally high abundance of up to 4 wt.% of S on the surface of Mercury (Nittler et al., 2011; Weider et al., 2015) is important for constraining the planets bulk composition (Nittler et al., 2018), its internal structure and geological history (Denevi et al., 2018). The high S abundance was attributed to a high sulfur solubility in highly reduced magmas (Namur et al.,

2016a; Zolotov et al., 2013) or transport of sulfide melt droplets from a mantle source (Malavergne et al., 2014). These hypotheses assume that the observed S occurs dissolved in magmatic rocks or as sulfides crystallized from the magma, and require very low oxygen fugacities of 3 to 7 logfO_2 units below the iron-wüstite buffer (IW-3 to IW-7) (McCubbin et al., 2012; Namur et al., 2016a). The oxygen fugacity relative to the IW buffer in this case, relates to the mantle sources of the basalts and not the surface for which we have chemical data from MESSENGER. These highly reducing conditions were derived from the observed low FeO concentration at the surface, the size of the core, and the S abundance, assuming S was dissolved in the basalts (Cartier and Wood, 2019; McCubbin et al., 2012; Namur et al., 2016a; Nittler et al., 2018). However, pyroclastic volcanic deposits on Mercury may be depleted in S and C, suggesting that the volcanic melts have lost substantial amounts of S and other volatiles upon eruption. This is evident in the S and C depletion in Nathair Facula (NE Rachmaninoff), the only pyroclastic deposit large enough to have its composition measured by MESSENGER (Deutsch et al., 2021; Pegg et al., 2021; Weider et al., 2016). Since the solubility of S in basalts increases with decreasing fO_2 from IW-3 to IW-7 (Anzures et al., 2020b; Namur et al., 2016a; O'Neill and Mavrogenes, 2002), the amount of S released by volcanic degassing from erupted volcanic plains is approximately an order of magnitude larger at IW-3 compared to IW-7 (Deutsch et al., 2021). The resulting volcanic gas in the system C-O-S was likely dominated by the species CO, S_2, CS_2, and COS (Zolotov et al., 2013; Zolotov, 2011), which is similar to a lunar volcanic gas (Renggli et al., 2017). Volcanogenic S may also be associated with the formation process of the Mercury hollows, which are currently active geological features (Blewett et al., 2018, 2013; Thomas et al., 2014). A number of processes have been proposed for the formation of these depressions. They include mobilization of volatiles (sulfides or graphite) by space weathering and thermal decomposition (Blewett et al., 2018; Helbert et al., 2013; Thomas et al., 2016; Vilas et al., 2016), solar heating in highly radiation exposed areas (Blewett et al., 2013; Thomas et al., 2014), or the oxidation and volatilization of graphite (Blewett et al., 2016).

Sulfur-bearing gases at high temperatures are highly reactive. At high oxygen fugacities such as in volcanic gases on Earth or Mars, SO_2 is the dominant S-bearing gas species and may react with

silicate glasses (Renggli and King, 2018) and minerals (King et al., 2018) to form sulfates and metal oxides. At reducing conditions relevant to Mercury (i.e., below the IW buffer), gas-solid reactions between S-rich reduced gases instead form sulfides (Renggli et al., 2019). For example, sulfidation reactions at reducing conditions occurred in lunar rocks returned by the Apollo missions, where troilite and pyroxene intergrowths replace olivine (Shearer et al., 2012).

Here, we present the results of experiments in evacuated silica glass tubes, simulating the reaction of reduced S-rich gas with Mercury-composition glasses and supercooled melts at 800, 1000, and 1200 °C. We use three glasses with compositions representing the high-Mg region, the low-Mg region of the northern volcanic plains, and high-Al region southwest and southeast of the northern volcanic plains (Table 1) (Namur and Charlier, 2017; Vander Kaaden et al., 2017), to test the viability of gas-solid reactions in the formation of sulfides and S enrichment in terranes with different chemical compositions.

Methods

We synthesized the low-Mg, high-Mg, and high-Al glasses with Mercury compositions (Table 1) (Namur and Charlier, 2017; Vander Kaaden et al., 2017) from reagent grade oxides (SiO_2, TiO_2, Al_2O_3, Fe_2O_3, and MgO) and carbonates ($CaCO_3$, $MnCO_3$, Na_2CO_3, and K_2CO_3). After decarbonation in air at 1000 °C for two hours, the mixtures were melted at 1450 °C in air. This oxidized glass was reground and melted again in a graphite crucible and in pure CO atmosphere (at the G-CO redox buffer) for 24 h at 1450 °C (Morlok et al., 2021). In all three glasses Fe formed metal nuggets, resulting in a low FeO content measured by microprobe (Table 1).

The Mercury glasses were placed in graphite cups and inserted into silica glass tubes with an inner diameter of 4 mm and a wall thickness of 1 mm. 0.0015g of elemental S was filled in graphite cups and placed below the sample cups, separated by SiO_2 glass wool (Fig. 1). The 4 cm long tubes were sealed under a vacuum of 10^{-5} bar. The experiments were suspended in a vertical tube furnace with a 6 cm long hot zone with internal temperature variations of less than 3 °C (Renggli and Klemme, 2020). The experiments were run for 24 h at 800, 1000, and 1200 °C. At these temperatures the

elemental S formed a gas, filling the tube and resulting in an initial pressure of ~12 bar, assuming that all S forms a gas. This S_2-rich gas reacted with the silicate glass samples in the upper graphite cup. The graphite present in the assembly buffered the fO_2 at the G-CO buffer (Renggli and Klemme, 2021). The silica glass tubes were lifted out of the vertical tube furnace and quenched in water. The reacted glass surfaces were imaged on a JSM-6510 Series Scanning Electron Microscope (SEM) in the low-vacuum mode at 50 Pa. Following this initial characterization the samples were cross-cut, mounted in epoxy resin and polished without water to avoid sample alteration, to a 0.25 µm grain size in anhydrous ethanol.

Major and minor element compositions of the experimental phases were performed with a JEOL JXA 8530F electron microprobe operated at 15 keV accelerating voltage and 15 nA beam current. The compositions of the altered glasses and the sulfide coatings were analyzed with a probe current of 60 nA and spot sizes of up to 10 µm, depending on the grain size. Prior to quantitative analyses all elements were standardized on natural and synthetic reference materials (supplementary material). To validate analytical precision and accuracy a set of secondary standards were analyzed and obtained results that generally match published values. Since the position of S X-ray emissions changes depending on the chemical bonding, SKα peaks were carefully determined performing qualitative wavelength scans for all samples prior to quantitative analyses. Semi-quantitative chemical maps were done at 15 kV, 80 nA using a focused electron beam, the dwell time was set to 80 ms, and the step size varied for individual maps between 0.1 and 0.5 µm. All further analytical details are shown in the supplemental excel table.

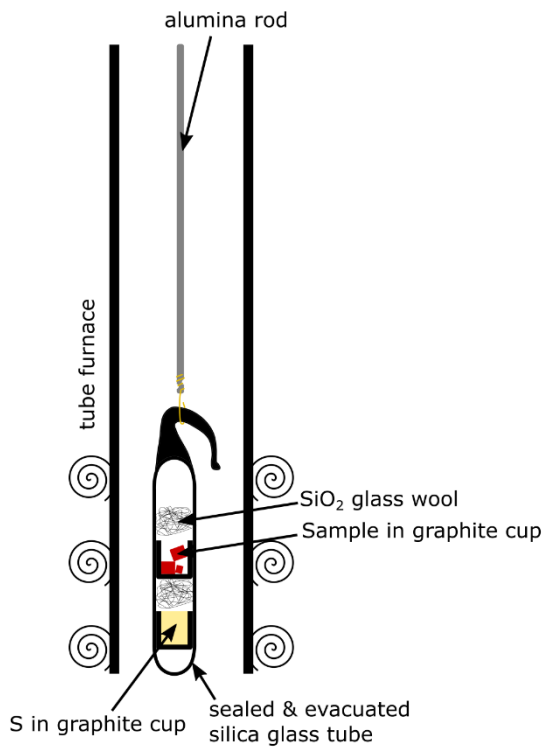

Figure 1: Experimental set-up of a double cup assembly in an evacuated silica glass tube. The sample glasses are in a graphite cup, which is placed above a second graphite cup loaded with elemental S. The sealed silica glass tube has an inner diameter of 4 mm and is 4 cm long. The tube was sealed under a vacuum of 10^{-5} bar.

Table 1: Compositions (wt.%) of the glasses used for the experiments measured by electron microprobe (10 measurements on each glass) (ID174 low-Mg IIA, ID156 high-Mg 1, ID155 high-Al from Morlok et al., 2021). The glass compositions represent the low-Mg region of the northern volcanic plains, the high-Mg region, and the high-Al region in the southwest and southeast of the northern volcanic plains (Namur and Charlier, 2017; Vander Kaaden et al., 2017). Standard deviations are given in brackets.

	low-Mg (ID 174)	high-Mg (ID 156)	high-Al (ID 155)
SiO_2	64.26(32)	56.01(38)	57.06(19)
TiO_2	0.46(02)	1.08(01)	1.39(08)
Al_2O_3	14.30(10)	10.80(14)	16.55(11)
FeO	0.05(08)	0(0)	0.07(03)
MnO	0.16(02)	0.49(01)	0.70(04)
MgO	8.97(12)	23.11(45)	14.78(15)
CaO	6.81(08)	7.73(09)	6.05(10)
Na_2O	4.81(12)	1.16(02)	3.15(08)
K_2O	0.19(03)	0.13(02)	0.24(02)
Total	100.01	100.52	99.99

Experimental results

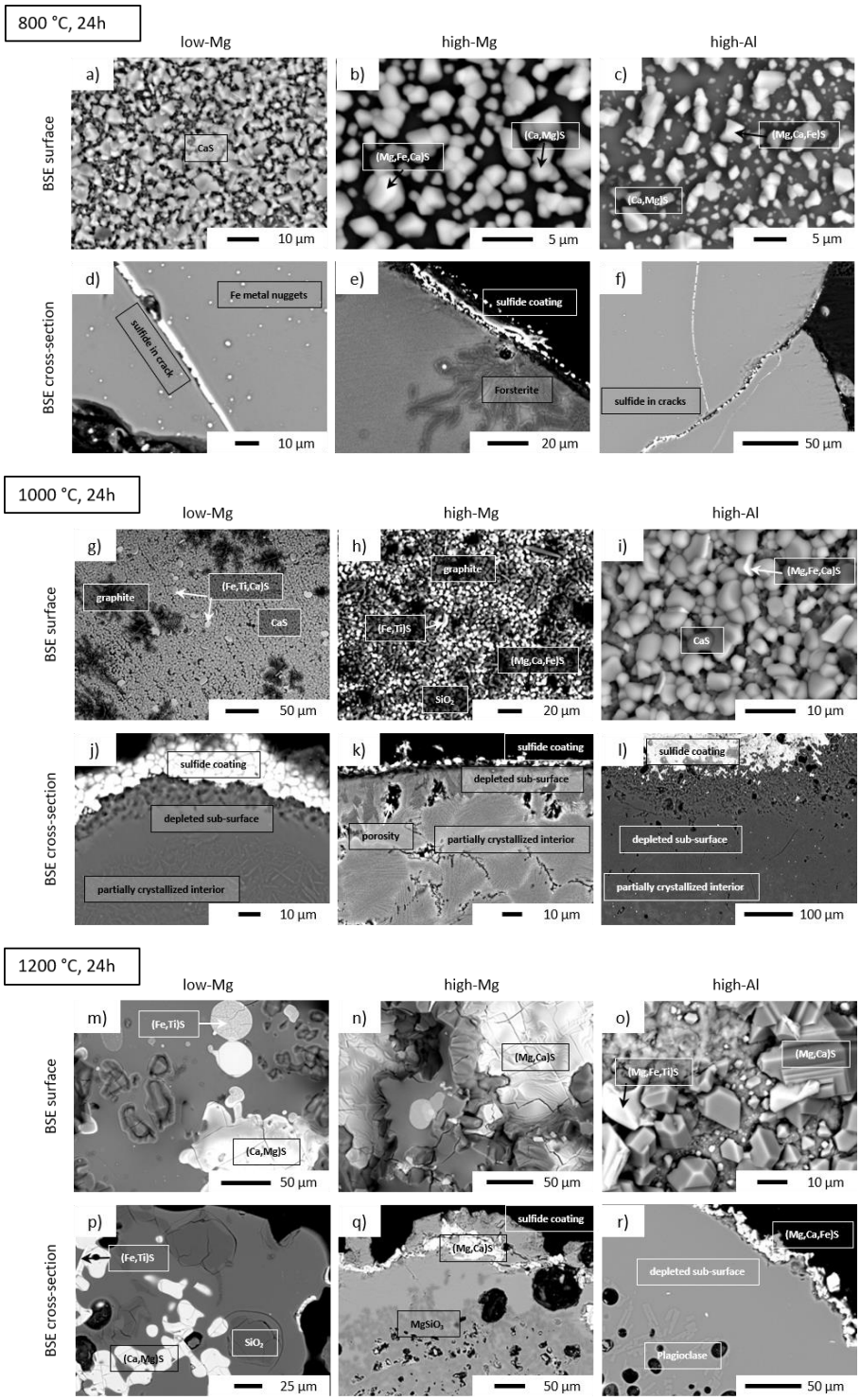

Figure 2: Back-scattered electron images (BSE) of the low-Mg (northern volcanic plains; a, d, g, j m, p), high-Mg (high-Mg region) (b, e, h, k, n, q) and high-Al (southeast and southwest of the northern volcanic plains) (c, f, i, l, o, r) Mercury glasses reacted at 800 °C (a-f), 1000 °C (g-l), and 1200 °C (m-r) for 24 h. Images a-c, g-i, and m-o show the sulfide coatings on the surfaces of the reacted glasses and images d-f, j-l, and p-r show the reacted samples in cross-section. The sulfidation reaction forms a mineral assemblage of sulfides and quartz in the coating, and a depleted and porous altered substrate.

The surfaces of the glasses processed at 800 and 1000 °C are covered by multi-phase coatings. Sulfide grain sizes range from 1 µm on the high-Mg glass reacted at 800 °C, to 15 µm on the low-Mg glass reacted at 1000 °C (Fig. 2). In addition, we observe a more complete coverage of the surface by the sulfide coating with increasing temperature. The Ca-rich sulfide forms a granular texture, whereas the Ti- and Fe-rich sulfides have platy morphologies. At 1200 °C the low-Mg and high-Mg compositions are above the glass transition temperatures and the sulfides are entrained into the silicate melts as immiscible sulfide melts. The high-Al sample has not entrained the sulfides, but the sulfides form a coating with grain sizes of up to 20 µm in diameter (Fig. 2). The compositions of the sulfides are systematically Mg-deficient relative to the glass compositions (Fig. 3). The low-Mg glass reacts to CaS at 800 and 1000 °C, whereas at 1200 °C we observe more Fe- and Ti-rich sulfides with [Ca/(Ca+Mg)] ~ 0.7. The sulfides formed in the high-Mg experiments show the largest variation of [Ca/(Ca+Mg)] from 0.27 to 0.95 (Fig. 3b). At 800 °C we observe a Fe-Ti-rich sulfide, CaS, and intermediate sulfide compositions with [Mg/(Mg+Fe+Ti] ~ 0.8 and up to 15 at.% Mn. At 1000 and 1200 °C the sulfides have lower Fe-concentrations and are more Mg-rich with [Mg/(Mg+Fe+Ti] ~ 0.9. The high-Al glass, which has intermediate Mg-contents between the low- and high-Mg glasses (Table 1), reacts to form Ca-rich sulfides at 800 and 1000 °C (Fig. 3c). In this system we do not observe any Fe- or Ti-rich sulfides, with [Mg/(Mg+Fe+Ti)] > 0.82 in all sulfides. At 1200 °C we observe the most Mg-rich sulfides of all experiments and the sulfide compositions approaches that of the high-Al glass composition in the Ca-Mg-Fe+Ti ternary system.

The glass substrates below the sulfide coatings become depleted in the sulfide-forming cations Ca, Fe, Mg, Ti, and Mn with increasing sulfidation. Cations that do not form sulfides, Si and Al in particular, become relatively enriched in the depleted zone, resulting in the crystallization of SiO_2 (e.g., Fig. 2). The depleted zone is characterized by the formation of porosity (Fig. 2 j-l), a common product of gas-solid reactions (King et al., 2018). The chemical zonation resulting from the sulfidation of the reacted glass surfaces is visualized in the electron microprobe elemental maps for the experiments at 800 °C in Fig. 4, 1000 °C in Fig. 5, and 1200 °C in Fig. 6. Below the depleted zone, the glasses, which were below the liquidus temperatures in all experiments, started to crystallize forsterite in the low- and

high-Mg experiments, enstatite in the high-Mg experiments, and plagioclase (~An60) and Mg-rich clinopyroxene in the high-Al experiment.

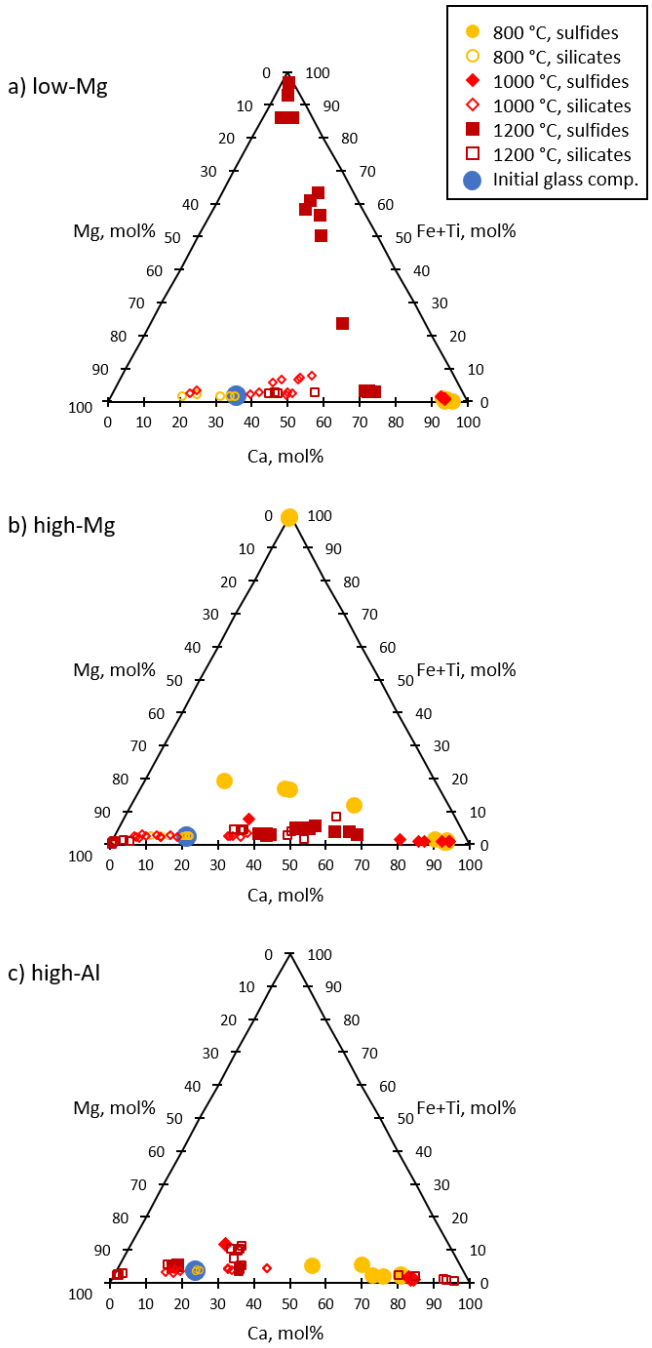

Figure 3: Ternary composition diagrams of the sulfide coatings normalized to the elemental system Mg-Ca-Fe+Ti in mol%. The large blue circles indicate the compositions of the synthetic glasses with a) low-Mg, b) high-Mg and c) high-Al compositions (Table 1). Yellow circles denote sulfide compositions at 800 °C, light-red diamonds at 1000 °C, and dark-red squares at 1200 °C. At 800 and 1000 °C the sulfides are enriched in Ca, Fe and Ti, relative to the respective glass composition.

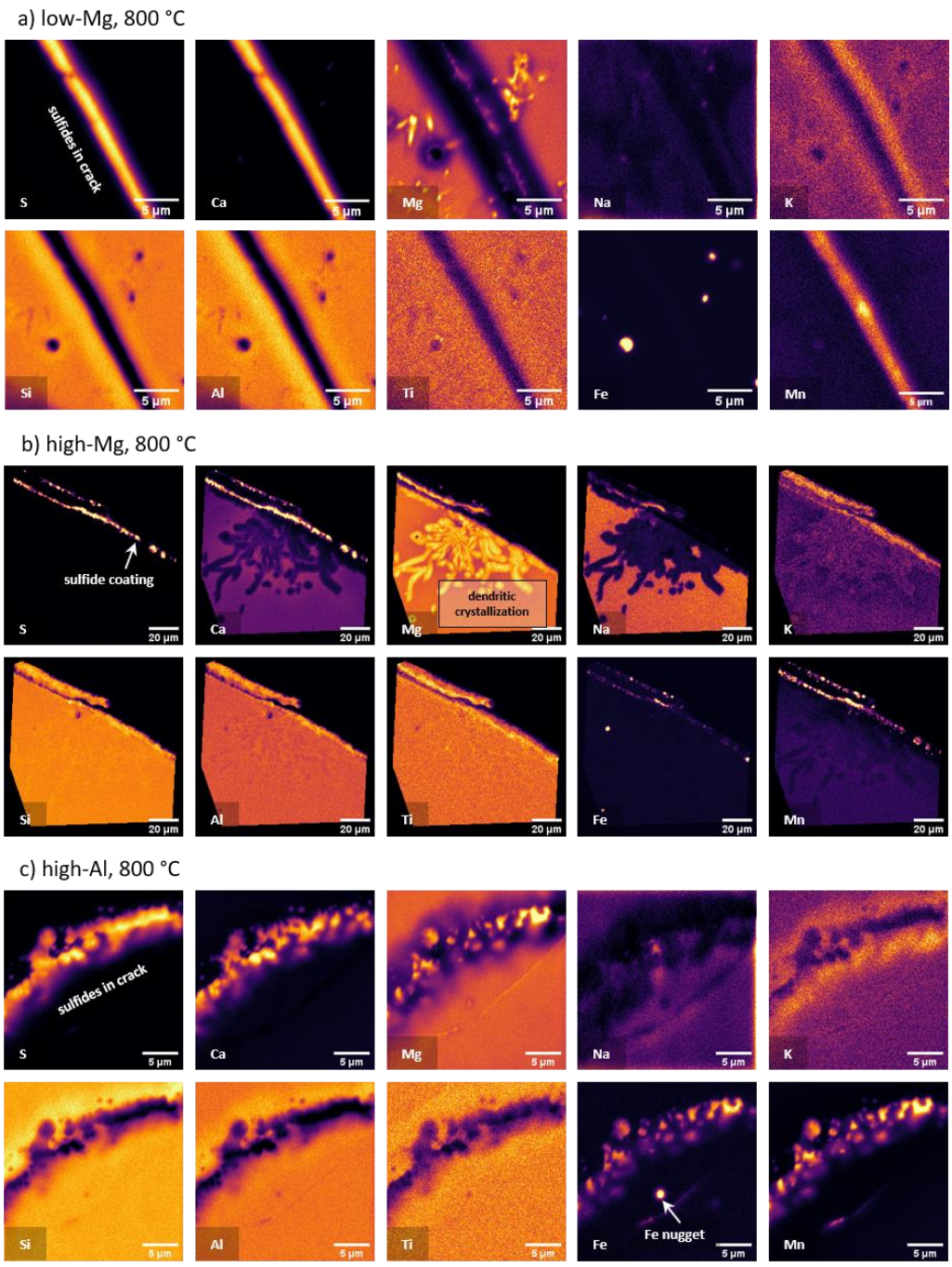

Figure 4: Electron microprobe maps of polished sample cross-sections of the reacted low-Mg (a), high-Mg (b) and high-Al (c) glasses at 800 °C for 24 h. The panels show semi-quantitative element distributions for S, Ca, Mg, Na, K, Si, Al, Ti, Fe and Mn. The maps show a cross-section from the surface sulfide coating (top) into the interior of the sample (bottom). Cation correlations with S identify the sulfide forming elements, including Ca, Mg, Ti and Fe, whereas Si, Al, and Na are retained in the altered glasses.

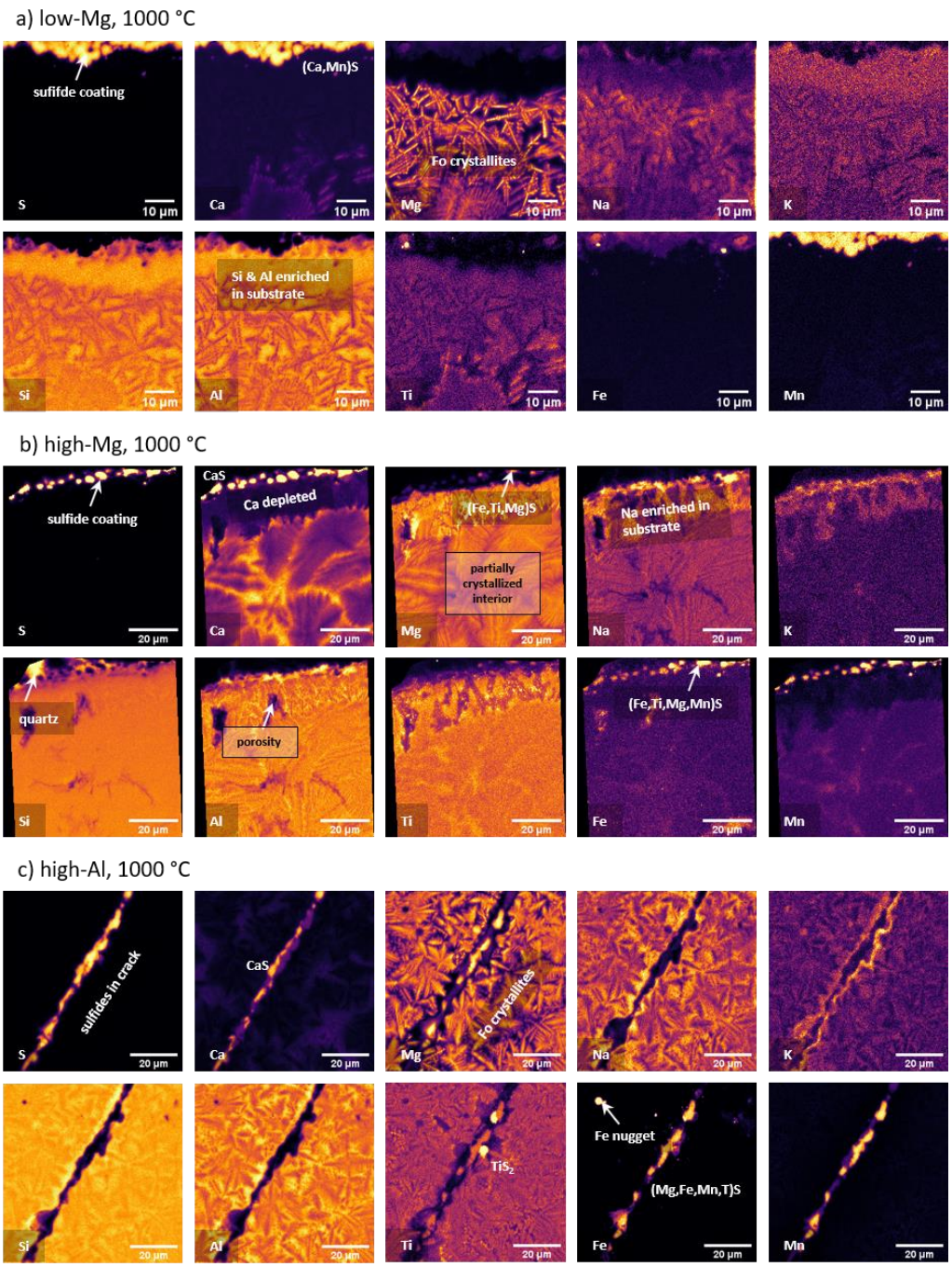

Figure 5: Electron microprobe maps of polished sample cross-sections of the reacted low-Mg (a), high-Mg (b) and high-Al (c) glasses at 1000 °C for 24 h. The panels show semi-quantitative element distributions for S, Ca, Mg, Na, K, Si, Al, Ti, Fe and Mn.

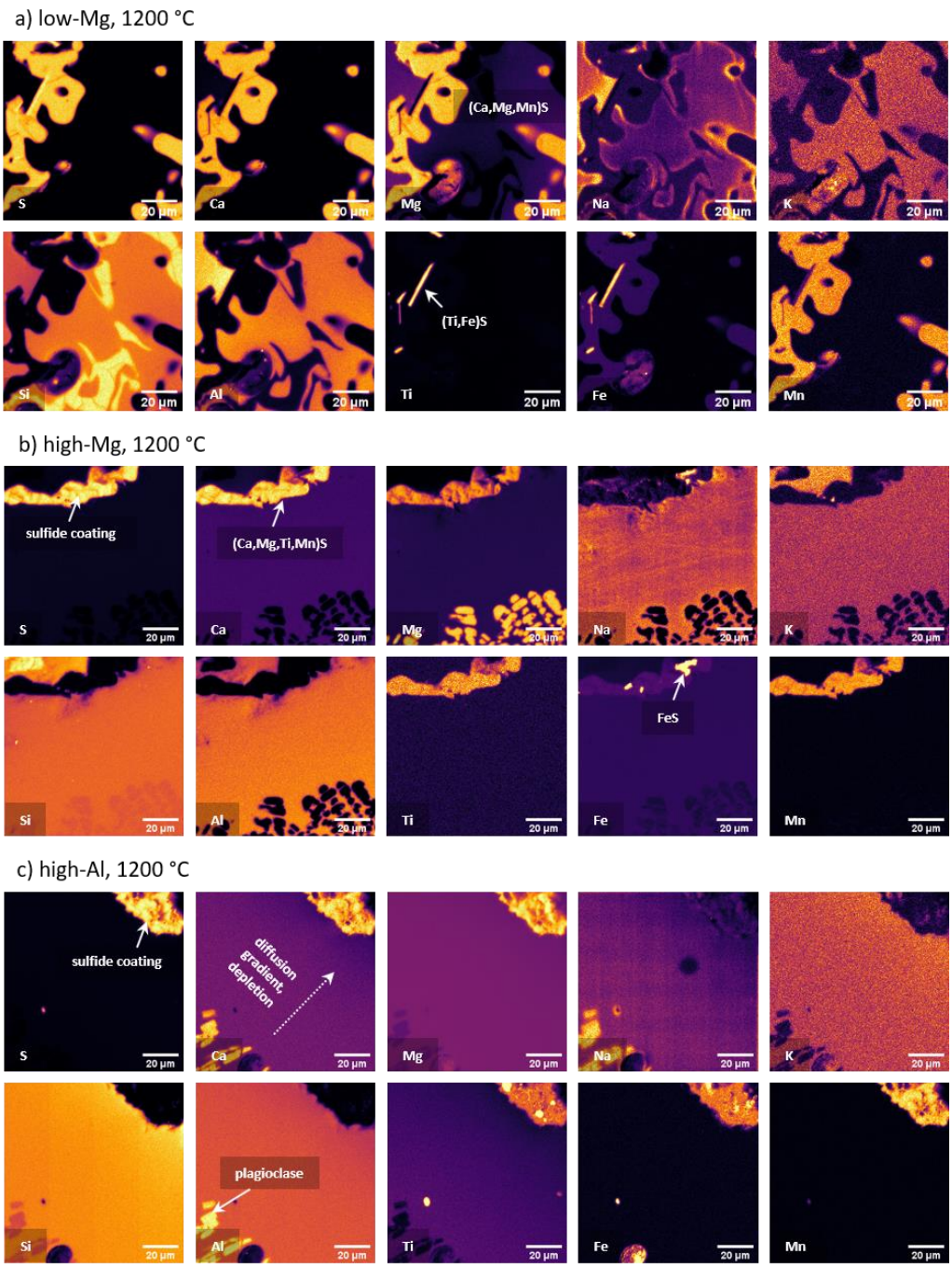

Figure 6: Electron microprobe maps of polished sample cross-sections of the reacted low-Mg (a), high-Mg (b) and high-Al (c) glasses at 1200 °C for 24 h. The panels show semi-quantitative element distributions for S, Ca, Mg, Na, K, Si, Al, Ti, Fe and Mn.

Discussion

The high S abundance measured by XRS (X-ray spectrometry) on the surface of Mercury has commonly been assumed to be hosted in magmatic rocks, dissolved in silicates or crystallized as sulfide phases (Anzures et al., 2020b, 2020a; Deutsch et al., 2021; Namur et al., 2016a, 2016b). This is based

on the increasing solubility of S in basaltic melts with decreasing oxygen fugacity (Anzures et al., 2020b; Namur et al., 2016a; O'Neill and Mavrogenes, 2002). These models suggest that the magmas on Mercury erupted highly reduced, at oxygen fugacities of IW-4 or lower, and crustal oxidation of the magmas was limited. Alternatively, moderate oxidation of the magmas from IW-7 to IW-3 prior to eruption would have reduced the solubility of S at 1350-1500 °C in silicate melts from ~7 wt.% to ~1 wt.% (Namur et al., 2016a; Zolotov et al., 2013), allowing extensive degassing of S.

A possible mechanism for the oxidation of a highly reduced, S-saturated magma is decompression, where CO becomes favored at pressures below 10 MPa, even at IW-5. The effect of decompression on fO_2 is small as noted by Zolotov (2011). However, the oxidation of graphite has been proposed to drive pyroclastic eruptions on the Moon (Fogel and Rutherford, 1995; Kerber et al., 2009), and may similarly play a role on Mercury. At oxygen fugacities below IW the magmas on Mercury were likely not buffered. As the magmas ascended to the surface the absolute fO_2 of the melt remained constant, and increased relative to the IW-buffer. On Earth, decompression of basaltic mantle sources causes the oxidation of the melts by up to four orders of magnitude relative to IW, from 10 GPa to ambient pressure, and crustal rocks are systematically more oxidized compared to the mantle (Foley, 2011). Similarly, decompression oxidation on Mercury could lower the solubility of S by several wt.% and this may in turn drive the degassing process. Finally, as magma rises through the crust, assimilation of TiO_2 and FeO bearing minerals could have further driven the oxidation of S-species in the melt (Zolotov, 2011).

As previously suggested, moderate oxidation from IW-7 to IW-3 leads to an increase of S degassing by an order of magnitude (Deutsch et al., 2021), which is in agreement with the observed depletion of S in pyroclastic deposits, formed by explosive eruptions driven by a S- and C-rich volcanic gas (Weider et al., 2016). Deutsch et al. (2021) estimated that a single volcanic eruption would have degassed enough volatiles to sustain a transient atmosphere from 250 up to 210,000 years. We argue that any volcanogenic S present in such a transient atmosphere will react rapidly with silicates to form sulfides and cause a S enrichment on the surface of Mercury.

The S-gas speciation varies as a function of the oxygen fugacity, temperature, pressure, and the C/S ratio in the gas phase (Zolotov, 2011). The two most abundant S-bearing gas species at reducing conditions below the IW buffer are S_2 and CS_2, followed by COS, CS, and S_3. Here, we consider how the two dominant gas species react with a Ca-, Mg- and Fe-bearing aluminosilicate melt to form sulfides, silicates, and release oxygen:

$$\{MgO + CaO + FeO + SiO_2 + Al_2O_3\}_{glass;\, melt;\, mineral} + 1.5S_{2(g)}$$
$$\rightarrow \{SiO_2 + Al_2O_3\}_{glass;\, melt;\, mineral} + 3(Mg, Ca, Fe)S + 1.5O_{2(g)}$$

In the presence of graphite, which is abundant in Mercury's crust (Peplowski et al., 2016; Vander Kaaden and McCubbin, 2015), the released oxygen will react to form $CO_{(g)}$. Alternatively, the reaction in a FeO poor system with the gas species CS_2 is:

$$\{MgO + CaO + SiO_2 + Al_2O_3\}_{glass;\, melt;\, mineral} + CS_{2(g)}$$
$$\rightarrow \{SiO_2 + Al_2O_3\}_{glass;\, melt;\, mineral} + 2(Mg, Ca)S + 2CO_{(g)}$$

We conducted experiments with melts and glasses of Mercury composition. However, the surface and crust likely consist primarily of crystalline phases. Crystallization experiments on Mercury basalt melts suggest that the primary mineralogy consists of anorthite (an), forsterite (fo), and diopside (di) (Namur and Charlier, 2017). The reaction of these minerals with a CS_2 gas is:

$$Mg_2SiO_4 + CaMgSi_2O_6 + 2CaSi_2Al_2O_8 + 3CS_{2(g)}$$
$$\rightarrow \{7SiO_2 + 2Al_2O_3\}_{glass;\, melt;\, mineral} + 3CaS + 3MgS + 6CO_{(g)}$$

As in the reaction of S_2 or CS_2 with basaltic Mercury glasses and super-cooled melts the minerals react to CaS, MgS, and aluminosilicate phases. This is in analogy to reactions at oxidizing conditions, where SO_2 reacts with glasses and minerals equally to form sulfates and aluminosilicates (King et al., 2018; Renggli et al., 2019; Renggli and King, 2018).

We conducted Gibbs free energy minimization calculations of a S-gas with an, fo, and di at 1000 °C and 1 bar, as a function of fO_2, using the software package HSC9 by Metso:Outotec (Fig. 7). We included the gas species SO_2, SO_3, SO, S_2O, COS, CS_2, CS, S_2, S_3, S_4, S_5, S_6, S_7, S_8, O_2, CO_2, CO,

and C in the calculation. The solid phases in the an sulfidation model are: $CaAl_2Si_2O_8$, CaS, SiO_2, Al_2O_3, $CaSO_4$, and $CaSO_3$; in the di sulfidation model: $CaMgSi_2O_6$, CaS, MgS, SiO_2, $CaSO_4$, $CaSO_3$, $MgSO_4$, and $MgSO_3$; in the fo sulfidation model: Mg_2SiO_4, MgS, SiO_2, $MgSO_4$, and $MgSO_3$. The initial condition of the calculation was set at 99 mol% SO_2 and 1 mol% of the silicate mineral (an, fo, di) respectively. Carbon was stepwise added at 1 mol% for 500 steps, to reduce fO_2, thereby decreasing the molar ratio of C/S from 0.88 at IW+2, 0.61 at IW, 0.44 at IW-3, and 0.41 at IW-5. The extent of this reaction, however, varies between the silicate minerals, where an reacts most extensively, followed by di and fo. With decreasing fO_2 fo remains the most resistant to sulfidation, but at reducing conditions relevant for Mercury, below IW, fo, an, and di are replaced by MgS, CaS, and SiO_2(+Al_2O_3) (Fig. 7). These calculations show, that the sulfidation of silicate minerals at reducing conditions results in the same alteration mineralogy as the sulfidation of the Mercury glasses demonstrated in the experiments.

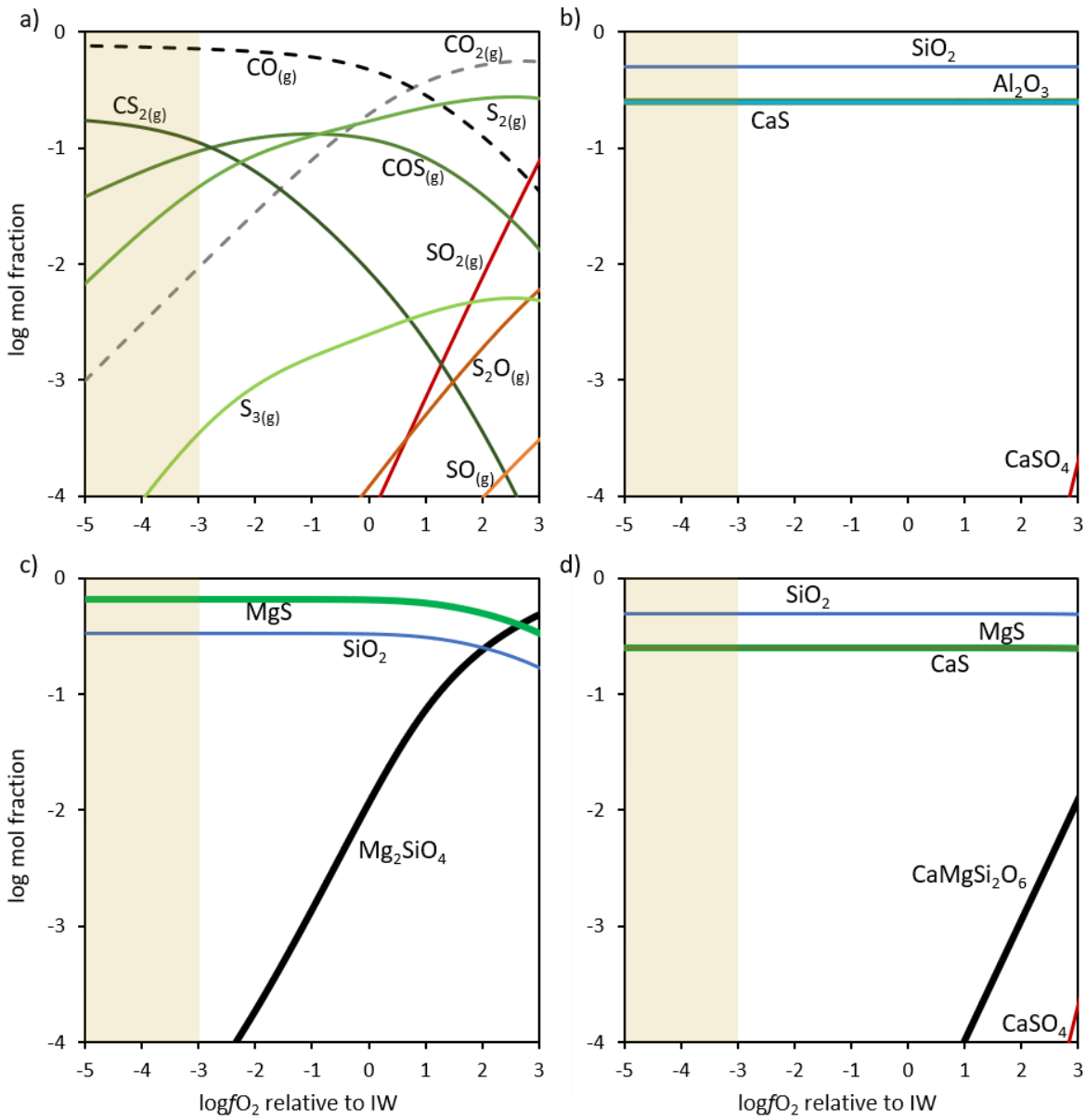

Figure 7: Gibbs free energy minimization calculations of equilibria between a S-rich gas (a) at 1000 °C and 1 bar shown in log mol fractions, as a function of oxygen fugacity from IW-5 to IW+3, with (b) anorthite, (c) forsterited, and (d) diopside. In the calculation the oxygen fugacity is varied by stepwise adding C to SO_2 gas. The molar ratio of S to the minerals remains constant, but the C/S ratio decreases with decreasing fO_2 from 0.61 at IW, to 0.44 at IW-3, 0.41 at IW-5. The mol fractions of the solids (b-d) are normalized to the total amounts of solids in each model. The shaded area indicates oxygen fugacities below IW-3, as estimated for magma source conditions on Mercury (McCubbin et al., 2012; Namur et al., 2016a). At these conditions, and in a S-rich system, the silicates an, fo, and di are not stable, and CaS, MgS, and aluminosilicates form instead.

Our experiments show that this type of gas-solid reaction forms sulfides efficiently under reducing conditions and at temperatures from 800 – 1200 °C at low pressures. Notably, we observe a varying chemical fractionation of the sulfide-forming cations (Ca, Mg, Fe), as the sulfide compositions change as a function of temperature and glass composition (Fig. 3), which is in agreement with thermodynamic investigations of these sulfide systems (Skinner and Luce, 1971). A key feature of this

type of gas-solid reaction, removing Ca, Mg, and Fe from the bulk glasses, is the relative enrichment of SiO_2 and Al_2O_3 in the altered glass substrate (Figs. 4-6). The relative enrichment in SiO_2 ultimately leads to the crystallization of quartz. As a consequence of this process the bulk composition a gas-solid reaction altered rock on the surface or in the crust of Mercury is not changed. Our model predicts mineral assemblages of sulfides with quartz and aluminosilicates, which differ fundamentally from petrological models, that posit the crystallization of forsterite in the high-Mg region, and forsterite, diopside, and plagioclase in the low-Mg region (Namur and Charlier, 2017; Vander Kaaden et al., 2017). This is in accordance with chemisorption alteration in terrestrial sub-volcanic environments, where the reaction between SO_2 gas and anorthite results in pervasive anhydrite and aluminosilicate formation (King et al., 2018).

The rate and degree of reaction in these gas-solid reactions is limited by a number of variables. First, the concentration and flux of S-rich gas determines the upper limit of sulfide formation and depends on the concentration of S in the magmatic source and the degree of oxidation and degassing in the crust, where oxidation is required to lower the solubility of S in the melt (Anzures et al., 2020b; Namur et al., 2016a). Second, the sulfide formation requires a diffusive flux of Ca, Mg, and Fe from silicate glasses and minerals to surfaces, grain boundaries, and cracks, where the reaction occurs. Analogous to SO_2 gas-solid reactions, this diffusion is likely the rate-limiting step (Renggli and King, 2018). A further limiting factor is the nucleation of SiO_2 in the Ca, Mg, and Fe depleted silicate, since the relative enrichment of SiO_2 below the surface reaction interface creates a self-inhibiting barrier, where the diffusivity of the sulfide cations is reduced (Renggli and King, 2018). Impact gardening of the crust and regolith (Costello et al., 2020) may further mobilize S and overcome kinetic limitations of the gas-solid reaction.

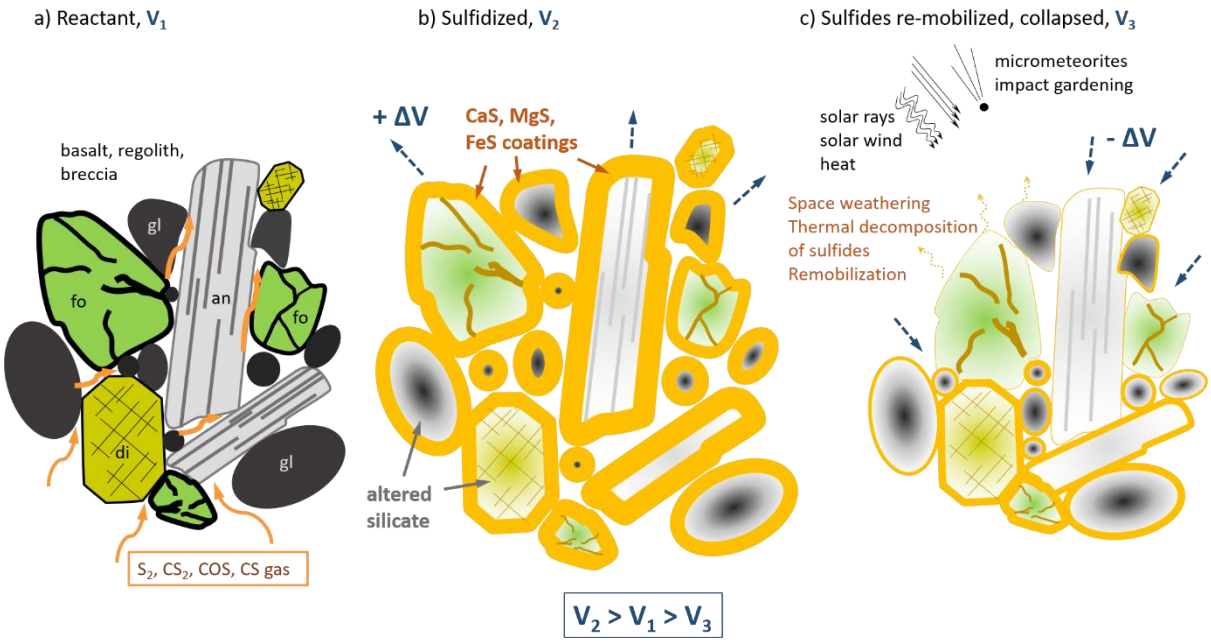

Figure 8: Schematic drawing of sulfidation the sulfidation process on the surface Mercury, followed by secondary sulfide re-mobilization and collapse, resulting in the development of hollows. a) basalt, regolith, breccias are permeated by S_2, CS_2, COS, CS gas resulting in the b) sulfidation of glass (gl), forsterite (fo), anorthite (an), and diopside (di) to primarily MgS and CaS, including the depletion of these elements in the altered silicates, which are enriched in SiO_2 and Al_2O_3. The sulfidation results in an overall volume increase (+ΔV). Secondary sulfide mobilization and decomposition by heat, radiation and impact gardening (Blewett et al., 2018; Helbert et al., 2013; Pieters and Noble, 2016; Thomas et al., 2014) results in c) volume decrease and collapse of the regolith/crustal material to form hollow depressions (modified from King et al., 2018 and Pieters & Noble 2016).

The sulfide coatings cause an overall volume increase in addition to the observed porosity in the modified silicates (Figs. 2 and 8). Where this alteration is pervasive along grain boundaries or along cracks, the altered rocks lose their structural integrity, leading to disruption of the regolith on Mercury. Sudden collapse may lead to further mobilization of volatile and moderately volatile components. We propose that this is a pathway to the formation of the Mercury hollows (Fig. 8). The hollows are surface features unique to Mercury and their origins remain enigmatic (Blewett et al., 2018, 2013; Thomas et al., 2014). They are irregularly shaped depressions with depths averaging around 24 m, most commonly found in low reflectance areas, that appear bright and bluish with diffuse borders (Blewett et al., 2018). Previously, hollows have been suggested to form by the loss of a volatile component, resulting in the compaction of the regolith (Thomas et al., 2016, 2014). Since hollows occur primarily on equator-facing slopes (Blewett et al., 2011; Thomas et al., 2014) space weathering induced by solar irradiation may cause decomposition of sulfides (Blewett et al., 2018). Alternatively, sulfides decompose due to thermal alteration (Helbert et al., 2013; Thomas et al., 2014). In regions where hollows are abundant, Mg, Ca,

and S are relatively enriched and correlated, suggesting the presence of CaS and MgS (Weider et al., 2012). The high reflectance of the bright hollow rims may be evidence for a secondary remobilization of sulfide-rich material (Barraud et al., 2020; Varatharajan et al., 2019; Wang et al., 2020). The alteration of volcanic rocks and regolith by gas-solid reactions, leading to collapse, remobilization, and hollow formation, provides a compelling explanation for these features that is consistent with the chemistry (Fig. 8).

Implications

In conclusion, our proposed mechanism for the origin of abundant oldhamite and niningerite on the surface of Mercury provides explanations for the S-rich surface, S depletion in degassed pyroclastic deposits, and the origin of sulfides in hollow-forming terranes. The process results in the concentration of S at the very surface of the planet. Extrapolating the high abundance of S observed at the surface by MESSENGER to deeper crustal basalts and the mantle would therefore result in an overestimation of the bulk S content of Mercury. We conducted gas-solid reaction experiments between a reduced S-rich gas and glasses with compositions representative for the low-Mg region of the northern volcanic planes, the high-Mg, and high-Al terranes on Mercury at 800-1200 °C over 24 hours. Over geologic timescales, and at the high surface temperatures of dayside Mercury, sulfidation reactions have caused an extensive enrichment of S on the planet's surface. Importantly, our reaction model makes mineralogical predictions, of the association of CaS, MgS, FeS, quartz, and aluminosilicates, that will be testable by the upcoming ESA/JAXA BepiColombo mission. Mid-Infrared spectroscopy observations (Hiesinger et al., 2020; Varatharajan et al., 2019) will allow the distinction of our predicted mineral assemblages, from those expected from previous petrological models suggesting forsterite, clinopyroxene, plagioclase, and sulfide assemblages (Namur and Charlier, 2017; Vander Kaaden et al., 2017).

Acknowledgements

CR is funded by the Deutsche Forschungsgemeinschaft (DFG, German Research Foundation) – project 442083018. This research was partially supported by DFG project 263649064 – SFB TRR-170

(publication number XXX). Our thanks go to M. Feldhaus, P. Weitkamp, L. Buxtrup, A. Hardes, S. Flunkert, B. Schmitte, and M. Trogisch for the help and support in the laboratories at the Institut für Mineralogie, at WWU Münster.

References

Anzures, B.A., Parman, S.W., Milliken, R.E., Lanzirotti, A., Newville, M., 2020a. XANES spectroscopy of sulfides stable under reducing conditions. Am. Mineral. 105, 375–381. https://doi.org/10.2138/am-2020-7146

Anzures, B.A., Parman, S.W., Milliken, R.E., Namur, O., Cartier, C., Wang, S., 2020b. Effect of sulfur speciation on chemical and physical properties of very reduced mercurian melts. Geochim. Cosmochim. Acta 286, 1–18. https://doi.org/10.1016/j.gca.2020.07.024

Barraud, O., Doressoundiram, A., Besse, S., Sunshine, J.M., 2020. Near-Ultraviolet to Near-Infrared Spectral Properties of Hollows on Mercury: Implications for Origin and Formation Process. J. Geophys. Res. Planets 125, e2020JE006497. https://doi.org/10.1029/2020JE006497

Blewett, D.T., Chabot, N.L., Denevi, B.W., Ernst, C.M., Head, J.W., Izenberg, N.R., Murchie, S.L., Solomon, S.C., Nittler, L.R., McCoy, T.J., Xiao, Z., Baker, D.M.H., Fassett, C.I., Braden, S.E., Oberst, J., Scholten, F., Preusker, F., Hurwitz, D.M., 2011. Hollows on Mercury: MESSENGER Evidence for Geologically Recent Volatile-Related Activity. Science 333, 1856–1859. https://doi.org/10.1126/science.1211681

Blewett, D.T., Ernst, C.M., Murchie, S.L., Vilas, F., 2018. Mercury's Hollows, in: Solomon, S.C., Nittler, L.R., Anderson, B.J. (Eds.), Mercury, The View After MESSENGER. Cambridge University Press, pp. 324–345.

Blewett, D.T., Stadermann, A.C., Susorney, H.C., Ernst, C.M., Xiao, Z., Chabot, N.L., Denevi, B.W., Murchie, S.L., McCubbin, F.M., Kinczyk, M.J., Gillis-Davis, J.J., Solomon, S.C., 2016. Analysis of MESSENGER high-resolution images of Mercury's hollows and implications for hollow formation. J. Geophys. Res. Planets 121, 1798–1813. https://doi.org/10.1002/2016JE005070

Blewett, D.T., Vaughan, W.M., Xiao, Z., Chabot, N.L., Denevi, B.W., Ernst, C.M., Helbert, J., D'Amore, M., Maturilli, A., Head, J.W., Solomon, S.C., 2013. Mercury's hollows: Constraints on formation and composition from analysis of geological setting and spectral reflectance. J. Geophys. Res. Planets 118, 1013–1032. https://doi.org/10.1029/2012JE004174

Cartier, C., Wood, B.J., 2019. The Role of Reducing Conditions in Building Mercury. Elements 15, 39–45. https://doi.org/10.2138/gselements.15.1.39

Costello, E.S., Ghent, R.R., Hirabayashi, M., Lucey, P.G., 2020. Impact Gardening as a Constraint on the Age, Source, and Evolution of Ice on Mercury and the Moon. J. Geophys. Res. Planets 125, e2019JE006172. https://doi.org/10.1029/2019JE006172

Denevi, B.W., Ernst, C.M., Prockter, L.M., Robinson, M.S., 2018. The Geologic History of Mercury, in: Solomon, S.C., Nittler, L.R., Anderson, B.J. (Eds.), Mercury, The View After MESSENGER. Cambridge University Press, pp. 144–175.

Deutsch, A.N., Head, J.W., Parman, S.W., Wilson, L., Neumann, G.A., Lowden, F., 2021. Degassing of volcanic extrusives on Mercury: Potential contributions to transient atmospheres and buried polar deposits. Earth Planet. Sci. Lett. 564, 116907. https://doi.org/10.1016/j.epsl.2021.116907

Evans, L.G., Peplowski, P.N., Rhodes, E.A., Lawrence, D.J., McCoy, T.J., Nittler, L.R., Solomon, S.C., Sprague, A.L., Stockstill-Cahill, K.R., Starr, R.D., Weider, S.Z., Boynton, W.V., Hamara, D.K., Goldsten, J.O., 2012. Major-element abundances on the surface of Mercury: Results from the MESSENGER Gamma-Ray Spectrometer. J. Geophys. Res. Planets 117. https://doi.org/10.1029/2012JE004178

Fogel, R.A., Rutherford, M.J., 1995. Magmatic volatiles in primitive lunar glasses: I. FTIR and EPMA analyses of Apollo 15 green and yellow glasses and revision of the volatile-assisted fire-fountain theory. Geochim. Cosmochim. Acta 59, 201–215.

Foley, S.F., 2011. A Reappraisal of Redox Melting in the Earth's Mantle as a Function of Tectonic Setting and Time. J. Petrol. 52, 1363–1391. https://doi.org/10.1093/petrology/egq061

Helbert, J., Maturilli, A., D'Amore, M., 2013. Visible and near-infrared reflectance spectra of thermally processed synthetic sulfides as a potential analog for the hollow forming materials on Mercury. Earth Planet. Sci. Lett. 369–370, 233–238. https://doi.org/10.1016/j.epsl.2013.03.045

Hiesinger, H., Helbert, J., Alemanno, G., Bauch, K.E., D'Amore, M., Maturilli, A., Morlok, A., Reitze, M.P., Stangarone, C., Stojic, A.N., Varatharajan, I., Weber, I., the MERTIS Co-I Team, 2020. Studying the Composition and Mineralogy of the Hermean Surface with the Mercury Radiometer and Thermal Infrared Spectrometer (MERTIS) for the BepiColombo Mission: An Update. Space Sci. Rev. 216, 110. https://doi.org/10.1007/s11214-020-00732-4

Kerber, L., Head, J.W., Solomon, S.C., Murchie, S.L., Blewett, D.T., Wilson, L., 2009. Explosive volcanic eruptions on Mercury: Eruption conditions, magma volatile content, and implications for interior volatile abundances. Earth Planet. Sci. Lett., MESSENGER's First Flyby of Mercury 285, 263–271. https://doi.org/10.1016/j.epsl.2009.04.037

King, P.L., Wheeler, V.M., Renggli, C.J., Palm, A.B., Wilson, S.A., Harrison, A.L., Morgan, B., Nekvasil, H., Troitzsch, U., Mernagh, T., Yue, L., Bayon, A., DiFrancesco, N.J., Baile, R., Kreider, P., Lipi, W., 2018. Gas–Solid Reactions: Theory, Experiments and Case Studies Relevant to Earth and Planetary Processes. Rev. Mineral. Geochem. 84, 1–56.

Malavergne, V., Cordier, P., Righter, K., Brunet, F., Zanda, B., Addad, A., Smith, T., Bureau, H., Surblé, S., Raepsaet, C., Charon, E., Hewins, R.H., 2014. How Mercury can be the most reduced terrestrial planet and still store iron in its mantle. Earth Planet. Sci. Lett. 394, 186–197. https://doi.org/10.1016/j.epsl.2014.03.028

McCoy, T.J., Peplowski, P.N., Mccubbin, F.M., Weider, S.Z., Solomon, S.C., Nittler, L.R., Anderson, B.J., 2018. The Geochemical and Mineralogical Diversity of Mercury, in: Mercury, The View After MESSENGER. Cambridge University Press, pp. 176–190.

McCubbin, F.M., Riner, M.A., Vander Kaaden, K.E., Burkemper, L.K., 2012. Is Mercury a volatile-rich planet? Geophys. Res. Lett. 39, L09202. https://doi.org/10.1029/2012GL051711

Morlok, A., Renggli, C., Charlier, B., Reitze, M.P., Klemme, S., Namur, O., Sohn, M., Martin, D., Weber, I., Stojic, A.N., Hiesinger, H., Joy, K.H., Wogelius, R., Tollan, P., Carli, C., Bauch, K.E., Helbert, J., 2021. Mid-infrared reflectance spectroscopy of synthetic glass analogs for mercury surface studies. Icarus 361, 114363. https://doi.org/10.1016/j.icarus.2021.114363

Namur, O., Charlier, B., 2017. Silicate mineralogy at the surface of Mercury. Nat. Geosci. 10, 9–13. https://doi.org/10.1038/ngeo2860

Namur, O., Charlier, B., Holtz, F., Cartier, C., McCammon, C., 2016a. Sulfur solubility in reduced mafic silicate melts: Implications for the speciation and distribution of sulfur on Mercury. Earth Planet. Sci. Lett. 448, 102–114. https://doi.org/10.1016/j.epsl.2016.05.024

Namur, O., Collinet, M., Charlier, B., Grove, T.L., Holtz, F., McCammon, C., 2016b. Melting processes and mantle sources of lavas on Mercury. Earth Planet. Sci. Lett. 439, 117–128. https://doi.org/10.1016/j.epsl.2016.01.030

Nittler, L.R., Chabot, N.L., Grove, T.L., Peplowski, P.N., 2018. The Chemical Composition of Mercury, in: Solomon, S.C., Nittler, L.R., Anderson, B.J. (Eds.), Mercury, The View After MESSENGER. Cambridge University Press, pp. 30–51.

Nittler, L.R., Starr, R.D., Weider, S.Z., McCoy, T.J., Boynton, W.V., Ebel, D.S., Ernst, C.M., Evans, L.G., Goldsten, J.O., Hamara, D.K., Lawrence, D.J., McNutt, R.L., Schlemm, C.E., Solomon, S.C., Sprague, A.L., 2011. The major-element composition of Mercury's surface from MESSENGER X-ray spectrometry. Science 333, 1847–1850. https://doi.org/10.1126/science.1211567

O'Neill, H.S.C., Mavrogenes, J.A., 2002. The Sulfide Capacity and the Sulfur Content at Sulfide Saturation of Silicate Melts at 1400°C and 1 bar. J. Petrol. 43, 1049–1087. https://doi.org/10.1093/petrology/43.6.1049

Pegg, D.L., Rothery, D.A., Balme, M.R., Conway, S.J., 2021. Explosive vent sites on Mercury: Commonplace multiple eruptions and their implications. Icarus 365, 114510. https://doi.org/10.1016/j.icarus.2021.114510

Peplowski, P.N., Klima, R.L., Lawrence, D.J., Ernst, C.M., Denevi, B.W., Frank, E.A., Goldsten, J.O., Murchie, S.L., Nittler, L.R., Solomon, S.C., 2016. Remote sensing evidence for an ancient carbon-bearing crust on Mercury. Nat. Geosci. 9, 273–276. https://doi.org/10.1038/ngeo2669

Pieters, C.M., Noble, S.K., 2016. Space weathering on airless bodies. J. Geophys. Res. Planets 121, 1865–1884. https://doi.org/10.1002/2016JE005128

Renggli, C.J., King, P.L., 2018. SO2 Gas Reactions with Silicate Glasses. Rev. Mineral. Geochem. 84, 229–255.

Renggli, C.J., King, P.L., Henley, R.W., Norman, M.D., 2017. Volcanic gas composition, metal dispersion and deposition during explosive volcanic eruptions on the Moon. Geochim. Cosmochim. Acta 206, 296–311. https://doi.org/10.1016/j.gca.2017.03.012

Renggli, C.J., Klemme, S., 2021. Experimental Investigation of Apollo 16 "Rusty Rock" Alteration by a Lunar Fumarolic Gas. J. Geophys. Res. Planets 126, e2020JE006609. https://doi.org/10.1029/2020JE006609

Renggli, C.J., Klemme, S., 2020. Experimental constraints on metal transport in fumarolic gases. J. Volcanol. Geotherm. Res. 400, 106929. https://doi.org/10.1016/j.jvolgeores.2020.106929

Renggli, Palm, A.B., King, P.L., Guagliardo, P., 2019. Implications of Reactions Between SO2 and Basaltic Glasses for the Mineralogy of Planetary Crusts. J. Geophys. Res. Planets 124, 2563–2582. https://doi.org/10.1029/2019JE006045

Shearer, C.K., Burger, P.V., Guan, Y., Papike, J.J., Sutton, S.R., Atudorei, N.-V., 2012. Origin of sulfide replacement textures in lunar breccias. Implications for vapor element transport in the lunar crust. Geochim. Cosmochim. Acta 83, 138–158. https://doi.org/10.1016/j.gca.2011.11.031

Skinner, B.J., Luce, F.D., 1971. Solid Solutions of the Type (Ca,Mg,Mn,Fe)S and their use as Geothermometers for the Enstatite Chondrites. Am. Mineral. 56, 1269–1296.

Thomas, R.J., Hynek, B.M., Rothery, D.A., Conway, S.J., 2016. Mercury's low-reflectance material: Constraints from hollows. Icarus 277, 455–465. https://doi.org/10.1016/j.icarus.2016.05.036

Thomas, R.J., Rothery, D.A., Conway, S.J., Anand, M., 2014. Hollows on Mercury: Materials and mechanisms involved in their formation. Icarus 229, 221–235. https://doi.org/10.1016/j.icarus.2013.11.018

Vander Kaaden, K.E., M. McCubbin, F., R. Nittler, L., N. Peplowski, P., Z. Weider, S., A. Frank, E., J. McCoy, T., 2017. Geochemistry, mineralogy, and petrology of boninitic and komatiitic rocks on the mercurian surface: Insights into the mercurian mantle. Icarus 285, 155–168. https://doi.org/10.1016/j.icarus.2016.11.041

Vander Kaaden, K.E., McCubbin, F.M., 2015. Exotic crust formation on Mercury: Consequences of a shallow, FeO-poor mantle. J. Geophys. Res. Planets 120, 2014JE004733. https://doi.org/10.1002/2014JE004733

Varatharajan, I., Maturilli, A., Helbert, J., Alemanno, G., Hiesinger, H., 2019. Spectral behavior of sulfides in simulated daytime surface conditions of Mercury: Supporting past (MESSENGER) and future missions (BepiColombo). Earth Planet. Sci. Lett. 520, 127–140. https://doi.org/10.1016/j.epsl.2019.05.020

Vilas, F., Domingue, D.L., Helbert, J., D'Amore, M., Maturilli, A., Klima, R.L., Stockstill-Cahill, K.R., Murchie, S.L., Izenberg, N.R., Blewett, D.T., Vaughan, W.M., Head, J.W., 2016. Mineralogical indicators of Mercury's hollows composition in MESSENGER color observations. Geophys. Res. Lett. 43, 1450–1456. https://doi.org/10.1002/2015GL067515

Wang, Y., Xiao, Z., Chang, Y., Cui, J., 2020. Lost Volatiles During the Formation of Hollows on Mercury. J. Geophys. Res. Planets 125, e2020JE006559. https://doi.org/10.1029/2020JE006559

Weider, S.Z., Nittler, L.R., Murchie, S.L., Peplowski, P.N., McCoy, T.J., Kerber, L., Klimczak, C., Ernst, C.M., Goudge, T.A., Starr, R.D., Izenberg, N.R., Klima, R.L., Solomon, S.C., 2016. Evidence from MESSENGER for sulfur- and carbon-driven explosive volcanism on Mercury. Geophys. Res. Lett. 43, 2016GL068325. https://doi.org/10.1002/2016GL068325

Weider, S.Z., Nittler, L.R., Starr, R.D., Crapster-Pregont, E.J., Peplowski, P.N., Denevi, B.W., Head, J.W., Byrne, P.K., Hauck, S.A., Ebel, D.S., Solomon, S.C., 2015. Evidence for geochemical terranes on Mercury: Global mapping of major elements with MESSENGER's X-Ray Spectrometer. Earth Planet. Sci. Lett. 416, 109–120. https://doi.org/10.1016/j.epsl.2015.01.023

Weider, S.Z., Nittler, L.R., Starr, R.D., McCoy, T.J., Stockstill-Cahill, K.R., Byrne, P.K., Denevi, B.W., Head, J.W., Solomon, S.C., 2012. Chemical heterogeneity on Mercury's surface revealed by the MESSENGER X-Ray Spectrometer: CHEMICAL HETEROGENEITY ON MERCURY. J. Geophys. Res. Planets 117, n/a-n/a. https://doi.org/10.1029/2012JE004153

Zolotov, M.Y., Sprague, A.L., Hauck, S.A., Nittler, L.R., Solomon, S.C., Weider, S.Z., 2013. The redox state, FeO content, and origin of sulfur-rich magmas on Mercury. J. Geophys. Res. Planets 118, 138–146. http://dx.doi.org/10.1029/2012JE004274

Zolotov, M.Yu., 2011. On the chemistry of mantle and magmatic volatiles on Mercury. Icarus 212, 24–41. https://doi.org/10.1016/j.icarus.2010.12.014